

# Reflected and transmitted waves from fault zones

Yaping Zhu and Roel Snieder

*Center for Wave Phenomena, Dept. of Geophysics, Colorado School of Mines, Golden, CO 80401*

## ABSTRACT

Waves reflected from and transmitted across fault zones can be used to extract information on those zones. Fault zones, characterized as either a low-velocity zone or fracture systems, modify the phase of the waveform and make the seismic response frequency dependent. In this paper we develop an extrapolation scheme for simulating fractures described as linear slip boundaries. Two  $9 \times 9$  linear systems need to be solved if the fracture stiffnesses and the background medium parameters are constant along the fractures. Numerical examples support the validity and efficiency of this approach. Based on the numerical simulation and theoretical arguments, we show that various internal properties of fault zones have differing influence on reflected waves. Fracture stiffness and fracture spacing change significantly the magnitude of the reflected waves, while small-scale random variation in velocity or fracture stiffness has little influence on the wavefields; hence fault zones with small-scale random variation can be modeled with equivalent media.

## 1 INTRODUCTION

Fault zones play a major role in accommodating the deformation in the Earth (structural geology and basin development), in determining the strength of Earth materials (mining applications), and in transporting or acting as barriers to fluid and gas (hydrocarbon exploitation). For a variety of applications, it is useful to determine the properties of fault zones remotely using wavefields.

The seismic description of a fault zone can be classified in terms of velocity change and fractures. A fault zone is usually thought to contain highly damaged material that has a lower velocity than do the surrounding rocks. Based on this, a number of studies have shown that waves can be guided along fault zones (Li et al., 1990; Li et al., 1994; Li and Vidale, 1996; Igel et al., 1997). Li and Vidale (1996) observed fault-zone guided waves and discussed the effects of overlaying sediments, fault zone step-overs, and hypocentral offset from the fault on the guided waves. Igel et al. (1997) and (2001) considered fault zones as low-velocity layers, and discussed various factors that influence trapped waves based on numerical simulation. They found that velocity variations along the fault zone alter significantly the trapping efficiency, while moderate geometric variations (e.g., changes in fault zone width) or small-scale scatterers do not.

Fractures have also been recognized as an important potential property of fault zones. In tight reservoir

rocks, fractures serve as major conduits for oil and gas (Yi et al., 1998; Schoenberg, 1998). Extensive laboratory work has been carried out for the seismic response of synthetic fractures (Pyrak-Nolte et al., 1990a) and natural fractures in rocks (Pyrak-Nolte et al., 1990b). A challenge is to extract the information on the geometrical and physical properties of fractures such as fracture strength, orientation, and spacing.

In addition to trapping waves, fault zones also generate reflected and transmitted waves. In this paper, we focus the discussion on reflected and transmitted waves from fault zones.

We analyze four basic models with different degree of complexity for characterizing fault zones. A fault zone can be modeled as 1) a low-velocity zone, 2) an idealized fracture, 3) a system of cracks, or 4) a complex shear zone that includes cracks, voids, and velocity perturbation. As stated in Schoenberg (1980), an idealized fracture is equivalent to a thin low-velocity layer with appropriate choice of layer thickness and impedance. In this paper, most emphasis is placed on fault zones characterized as fractures or cracks.

We develop an extrapolation scheme for the staggered-grid finite-difference simulation of fractures described as linear slip boundaries. In the update of the stresses at each time step in the region of fractures, particle velocities are extrapolated from neighboring points to the point where the stress needs to be evaluated. The difference between the extrapolated particle velocities

across the fracture gives time derivative of the stresses and for updating the stresses.

In the extrapolation scheme, two  $9 \times 9$  linear systems are designed for evaluating the particle velocities and stresses at the fracture interface. If the fracture stiffnesses and the background medium parameters are constant along the fractures, only two  $9 \times 9$  linear systems are required for all the fractures; otherwise different linear systems need to be solved for each grid point on the fractures where either the fracture stiffness or the background medium parameter changes. Since coefficient matrices in all those linear systems are time-invariant and need to be solved only once, extra computation cost for simulating the fractures is negligible. Numerical examples support the validity and efficiency of this approach.

Based on numerical simulation and theoretical arguments, we find that the internal properties of fault zones have various degrees of influence on reflected waves. For example, fracture stiffness and fracture spacing change significantly the magnitude of the reflected waves. As the fracture stiffness increases to infinity, the fracture behaves as a welded interface, but as the fracture stiffness decreases to zero, the fracture degenerates to a pair of free surfaces. For fault zones modeled as a system of cracks oriented perpendicular to the wavefront, waves propagate as if there is no crack and hence no reflected wave is excited. Other properties such as small-scale random variation in the fault zone have little influence on the wavefields; hence fault zones can be modeled with equivalent media.

The paper is organized as follows. In the next section, we introduce various types of models for characterizing fault zones and discuss the analytic solution for reflection and transmission coefficients from an idealized fracture. We then propose an extrapolation scheme for the simulation of fractures and test the approach by comparing the numerical results with the analytic solution for an idealized fracture. In the final section, we investigate various properties of the wavefields, including fracture stiffness, fracture spacing, crack distribution pattern, and random variation.

## 2 THEORETICAL BACKGROUND

### 2.1 Models for characterizing fault zones

Fault zones can be characterized by models in order of increasing complexity (Figure 1): 1) a low-velocity zone, 2) an idealized fracture, 3) a system of cracks, and 4) a complex shear zone.

A fracture is a non-welded interface across which the tractions are continuous while the displacements are discontinuous. A simple way to describe the displacement discontinuity is the elastic boundary condition,

$$\tau_{zz} = \mathcal{K}_z(u_z^{II} - u_z^I), \quad \tau_{zz}^{II} = \tau_{zz}^I,$$

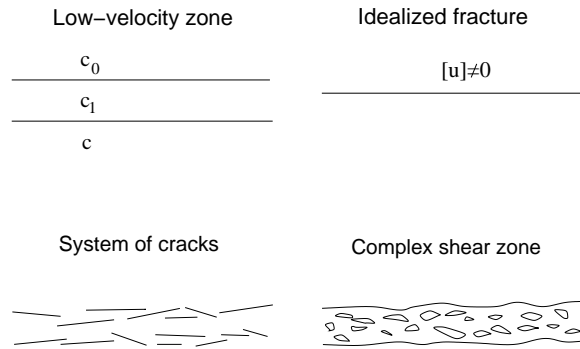


**Figure 1.** Four models of fault zones with varying degree of complexity.

$$\begin{aligned} \tau_{xz} &= \mathcal{K}_x(u_x^{II} - u_x^I), & \tau_{xz}^{II} &= \tau_{xz}^I, \\ \tau_{yz} &= \mathcal{K}_y(u_y^{II} - u_y^I), & \tau_{yz}^{II} &= \tau_{yz}^I, \end{aligned} \quad (1)$$

where the fracture interface is in the horizontal  $x - y$  plane, the  $z$  axis is perpendicular to the fracture interface,  $u$  and  $\tau$  are the particle displacement and stress, respectively, and  $\mathcal{K}$  is the fracture stiffness (in units of Pa/m), which is an indicator of the strength of the fracture. The elastic boundary condition is also denoted as a linear-slip interface condition (Schoenberg, 1980; Fan et al., 1996; Schoenberg, 1998; Myer, 1998), which is valid when the thickness of the fracture is much smaller than the dominant wavelength of the seismic wave. Hence we consider an idealized fracture as having zero thickness in the context of linear slip theory.

A more complicated model of the fault zone is a system of cracks possibly with varying length scales and strengths. The cracks typically have a certain dominant orientation. Here we limit the discussion to parallel cracks. More complicated fault zones result from complex shearing. Such zones consist of many fractures, with velocity and strength variation, and the presence of fault gouge and fluids.

### 2.2 Reflection and transmission coefficients of an idealized fracture

The reflection and transmission coefficients of SH-waves that interact with a planar infinite fracture are given by

$$\dot{S}\dot{S} = \frac{1 - i\Delta - \frac{\rho_2\beta_2 \cos j_2}{\rho_1\beta_1 \cos j_1}}{1 - i\Delta + \frac{\rho_2\beta_2 \cos j_2}{\rho_1\beta_1 \cos j_1}}, \quad (2)$$

$$\dot{S}\dot{S} = \frac{2}{1 - i\Delta + \frac{\rho_2\beta_2 \cos j_2}{\rho_1\beta_1 \cos j_1}}, \quad (3)$$

where

$$\Delta = \omega\rho_2\beta_2 \cos j_2 / \mathcal{K}_y, \quad (4)$$

subscripts 1 and 2 denote the media on both sides of the fracture,  $j$  is the angle that the raypath of the SH-waves

make with the normal to the fracture,  $\rho$  and  $\beta$  are the density and SH-wave velocity,  $\omega$  is the radial frequency, and  $i$  represents the imaginary unit.

The presence of the fracture is manifested in the factor  $\Delta$ , which depends on properties of the medium, the frequency of the wave, and more significantly, the fracture stiffness  $\mathcal{K}$ . Since  $\Delta$  appears in the combination  $i\Delta$ , both the reflection and transmission coefficients are complex numbers for all angles of incidence. Hence, the presence of a fracture changes both the amplitude and the phase of the waveform.

If there is no fracture,  $\Delta = 0$  and the expressions (2) and (3) degenerate to the familiar coefficients resulting from an impedance contrast. In that case, both the reflection and transmission coefficient are real valued and independent of frequency for incidence angle less than critical.

For the special case where the media on both sides of the fracture have the same density and velocity, expressions (2) and (3) simplify to

$$\dot{S}\dot{S} = \frac{-i\Delta}{2-i\Delta}, \quad \dot{S}\dot{S} = \frac{2}{2-i\Delta}. \quad (5)$$

Figure 2 shows the reflection coefficient for SH-waves at a velocity contrast across an interface and at an idealized fracture. In both cases, the density is constant:  $\rho_1 = \rho_2 = 1500 \text{ kg/m}^3$ . For the velocity contrast (Figure 2a), SH-wave velocities are  $\beta_1 = 1732 \text{ m/s}$  for the upper medium and  $\beta_2 = 1270 \text{ m/s}$  for the lower medium. For the fracture interface (Figure 2b), SH-wave velocity is constant across the interface, with  $\beta_1 = \beta_2 = 1732 \text{ m/s}$ , and the fracture stiffness  $\mathcal{K}_y = 2.096 \times 10^9 \text{ Pa/m}$ . In this test, the fracture stiffness has the same order of the magnitude as in Fan et al. (1996). Reasonable magnitudes for the fracture stiffness have also been discussed in Myer (1998) and Pyrak-Nolte and Morris (2000). For the influence of fracture stiffness on reflected waves, refer to section ‘‘Internal properties of fault zones’’ below.

For a pure velocity contrast, the reflection coefficient is independent of frequency. In contrast, for the idealized fracture the reflection coefficient varies substantially with frequency. For our choice of the fracture stiffness, the magnitude of the reflection coefficients is large (0.1 to 0.2), which means that with favorable source-receiver geometry these reflected waves can be observed in reflection data, perhaps better than reflection from impedance contrasts. Note that for the idealized fracture, the waveform changes because of the phase change which is also dependent on frequency.

The analytic formulas of the reflection and transmission coefficients for P- and SV-waves are provided in Chaisri and Krebes (2000). Figure 3 shows the reflection coefficients of P- and SV-waves excited at an idealized fracture. The medium parameters are: constant background velocity, P-wave velocity  $\alpha = 3000 \text{ m/s}$ , SV-wave velocity  $\beta = 1732 \text{ m/s}$ , and density  $\rho = 1500 \text{ kg/m}^3$ . The fracture stiffnesses are  $\mathcal{K}_z = 4.192 \times 10^9 \text{ Pa/m}$  and  $\mathcal{K}_x = 2.096 \times 10^9 \text{ Pa/m}$ . Although the an-

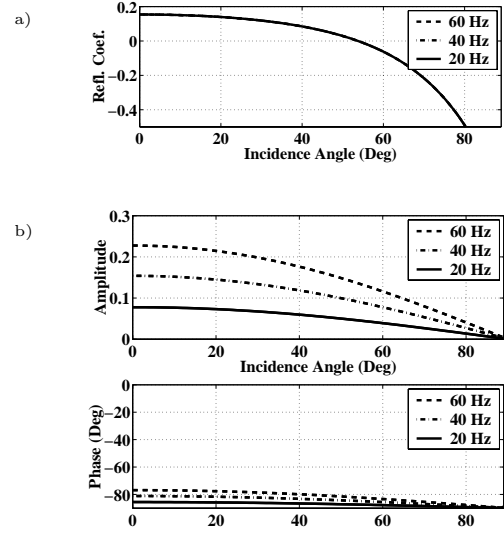


**Figure 2.** Reflection coefficients for SH-waves excited from: a) a velocity contrast interface and b) an idealized fracture interface. For the velocity contrast model, the medium parameters are SH-wave velocity  $\beta_1 = 1732 \text{ m/s}$  for the upper medium,  $\beta_2 = 1270 \text{ m/s}$  for the lower medium, and constant density  $\rho_1 = \rho_2 = 1500 \text{ kg/m}^3$ . For the fracture interface, the medium parameters are constant SH-wave velocity  $\beta_1 = \beta_2 = 1732 \text{ m/s}$ , constant density  $\rho_1 = \rho_2 = 1500 \text{ kg/m}^3$ , fracture stiffnesses  $\mathcal{K}_y = 2.096 \times 10^9 \text{ Pa/m}$ .

alytic forms of the reflection and transmission coefficients are more complicated for P- and SV-waves than for SH-waves, they also exhibit frequency dependence and phase change.

### 3 NUMERICAL SCHEME AND VERIFICATION

#### 3.1 Extrapolation scheme for simulating fractures

Although the analytic solution for scattered waves is known for a planar fracture, a stack of parallel fractures (Appendix B), and a finite crack (Sánchez-Sesma and Iturrarán-Viveros, 2001), the analytic solution for systems of fractures is hard to get, especially when the background medium is heterogeneous. Hence a numerical approach is required to assess wave propagation through fractures.

We developed an extrapolation scheme for simulating fractures described as linear slip boundaries (Appendix A). It is based on velocity-stress finite-differencing on a staggered-grid (Virieux, 1984; Virieux, 1986), which updates the particle velocities and stresses alternatively at each time step.

In our approach, two  $9 \times 9$  linear systems, expressions (A9) and (A10), are designed for evaluating the

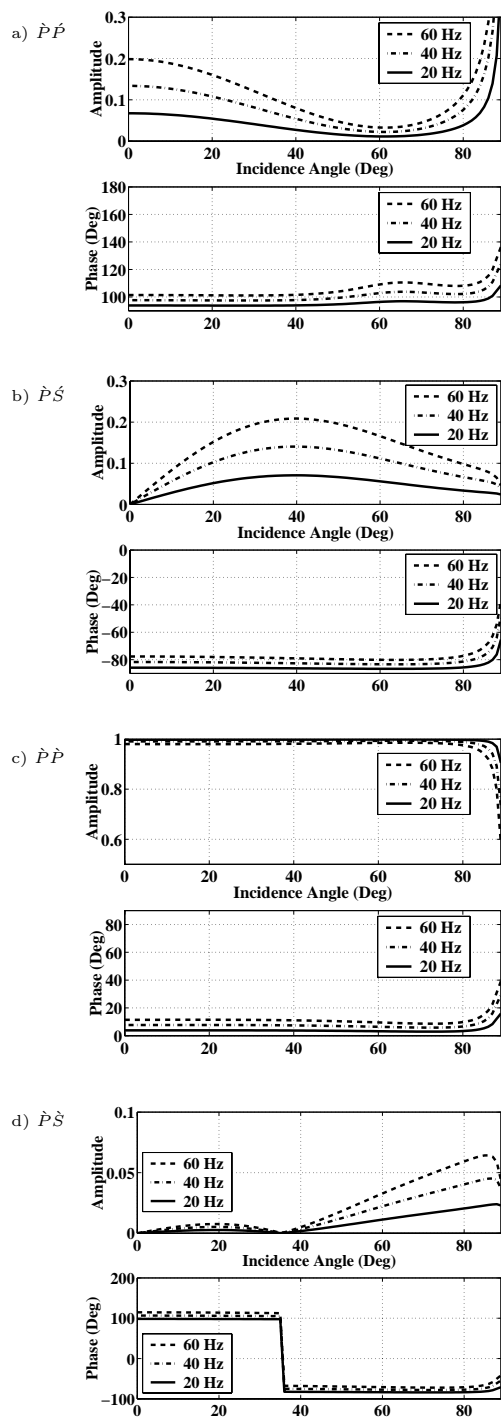


**Figure 3.** Reflection and transmission coefficients of waves excited from an idealized fracture: a)  $\hat{P}\hat{P}$ , b)  $\hat{P}\hat{S}$ , c)  $\hat{P}\hat{P}$ , and d)  $\hat{P}\hat{S}$ . The medium parameters are constant background velocity, P-wave velocity  $\alpha=3000$  m/s, SV-wave velocity  $\beta=1732$  m/s, and density  $\rho=1500$  kg/m<sup>3</sup>. The fracture stiffnesses are  $\mathcal{K}_z = 4.192 \times 10^9$  Pa/m and  $\mathcal{K}_x = 2.096 \times 10^9$  Pa/m.

particle velocities and stresses at the fracture interface, one for  $v_x$  and  $\tau_{xz}$  and another for  $v_z$  and  $\tau_{zz}$ . In the regions where the fracture is absent a standard staggered-grid scheme is applied. However, in the presence of horizontal fractures (in the x-direction), for each time step we update first the particle velocities  $v_x$  and  $v_z$  and the stress component  $\tau_{xx}$  in the same way as in a standard staggered-grid scheme, then we update the stress components  $\tau_{xz}$  and  $\tau_{zz}$  according to expressions (A9) and (A10).

Note that for fractures, wherever the fracture stiffnesses and the background medium parameters are constant along the fractures, only two  $9 \times 9$  linear systems are required; otherwise different linear systems need to be solved for each grid point on the fracture where either the fracture stiffness or the background medium parameters change. Fortunately, the coefficient matrices in both the linear systems are time-invariant, which means that we need to solve those matrices only once and use them for all the following time steps in the simulation. Thus the extra computation cost for simulating the fractures is negligible.

### 3.2 Numerical example and verification

To test the validity of the finite-difference code, we consider P-SV waves in a two-layer model with an idealized planar fracture embedded in constant background media (Figure 4). An idealized planar fracture is placed at a depth of 2000 m. The fracture stiffnesses are set as  $\mathcal{K}_z = 1.2985 \times 10^9$  Pa/m and  $\mathcal{K}_x = 5.2564 \times 10^9$  Pa/m. The grid spacing is 5 m, the time step is 0.25 ms, and the number of grid points in the test example is  $1201 \times 1401$ . A P-wave was excited from a point source at the position marked by an asterisk. The source wave is a Ricker wavelet with the dominant frequency of 12 Hz. An array of receivers is located at a depth of 1800m, with horizontal offsets extending from -500 m to 500 m. Another array of receivers is located below the source, with the depth extending from 1800 m to 2200m to record snapshots of the waves propagating through the fracture. In Igel et al. (2001), the number of points per dominant wavelength is set as 20 in the numerical simulation of fault zones characterized as low-velocity zones. In our numerical test, we recommend that within the fracture region the number of points in the dominant wavelength be set at  $\geq 40$ .

In Figure 5, we show snapshots of the modeled vertical particle velocity  $v_z$  and normal stress  $\tau_{zz}$  across the fracture. The P-wave propagates through the fracture at the depth of 2000 m at normal incidence. Discontinuity is visible for  $v_z$  across the fracture, while  $\tau_{zz}$  is continuous across the fracture. The figure clearly shows how a fracture is modeled as a linear-slip boundary condition.

Figure 6 a) shows the modeled PP reflected field at normal incidence. Compared to the analytical solution for the PP reflection at normal incidence (Chaisri and

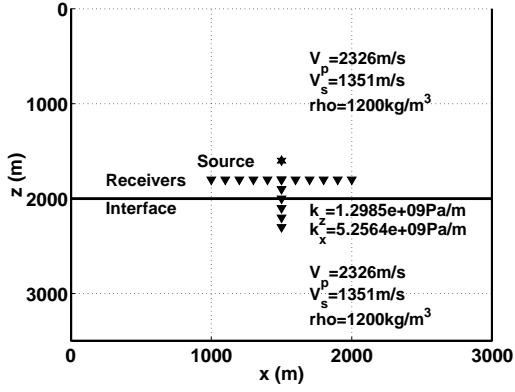


**Figure 4.** Geometry of the model with an idealized planar fracture.

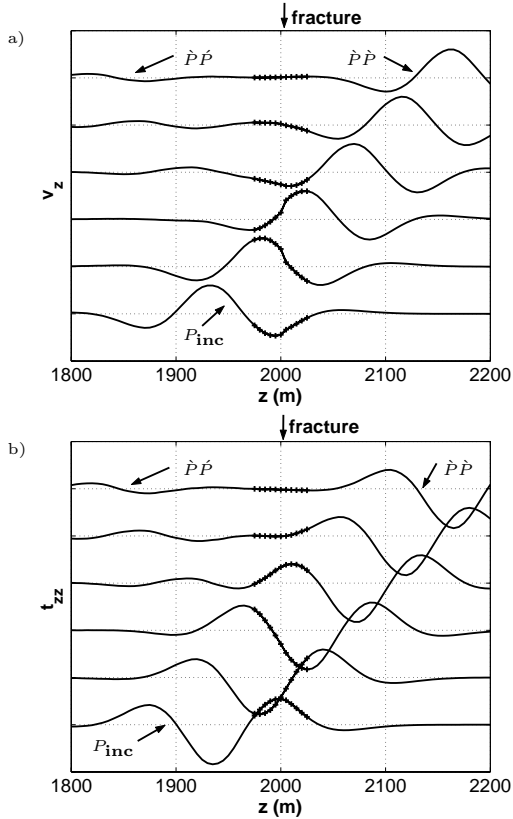


**Figure 5.** Different space-time snapshots of a) the normalized vertical component of the particle velocity  $v_z$  and b) the normal stress  $\tau_{zz}$ , during the wave propagation through a fracture at normal incidence. The difference in time between subsequent plots is 0.02 s. The fracture is located at the depth of 2000 m and the vertical grid spacing in the simulation is 5 m. Discontinuity is observed for  $v_z$  across the fracture, while  $\tau_{zz}$  keeps continuous across the fracture. Waveforms near the fracture are highlighted with the plus sign (+).

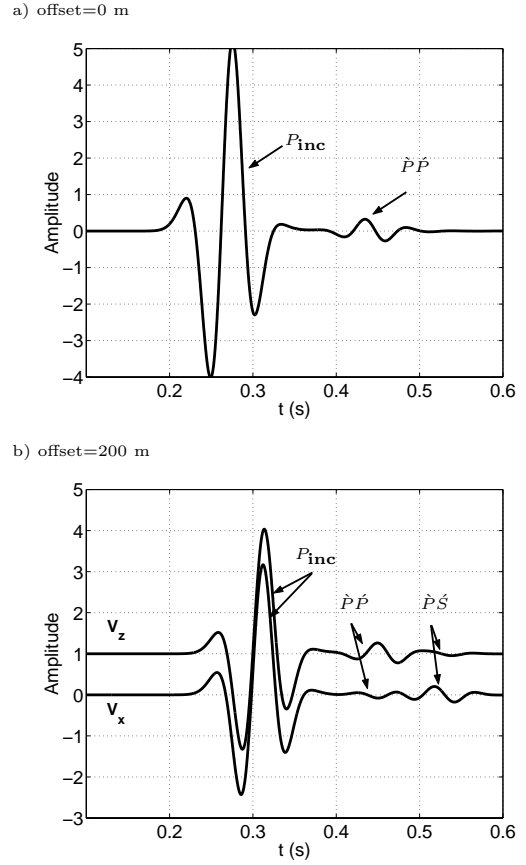


**Figure 6.** Waveforms of PP and P-SV reflections: a) offset=0 m and b) offset=200 m. For offset=200 m, the lower trace is the  $x$ -component of the particle velocity,  $v_x$ , and the upper trace is the  $z$ -component of the particle velocity,  $v_z$ . Receivers are located at the depth of 1800 m.

Krebes, 2000), the error of the peak amplitude in the numerical simulation is less than 5%. For larger offset, as shown in Figure 6 b), the particle polarization for PP and P-SV reflections needs to be considered in order to evaluate the amplitude of PP and P-SV reflections from  $x$ - and  $z$ -component data. Comparison between the numerical and analytic solution also indicates the validity of the finite difference scheme in simulating waves excited by fractures.

### 3.3 Further discussion

Currently, a popular way to model wave propagation in fractures is to use an equivalent medium to represent a fracture (Igel et al., 1997; Coates and Schoenberg, 1995), e.g., a low-velocity layer. Schoenberg (1980) discussed the equivalence between a thin low-velocity layer and an idealized fracture. The underlying assumptions for the equivalence between the low-velocity layer and the fracture are: 1) the thickness of the low-velocity layer

should be much smaller than the wavelength; 2) the impedance in the layer should be much smaller than that in the background media.

The advantage of the low-velocity-layer model in finite-difference simulation is that it requires no special treatment of the boundary conditions. However, since it requires the thickness to be much smaller than the wavelength and the impedance in the layer to be much smaller than that in the background media, both grid size and the time step must be very small. In our approach, in the regions of fractures 40 grid points per dominant wavelength are good enough to model waveforms of the reflection and transmission accurately.

To make the extrapolation stable for a fracture, other fractures should not be present at neighboring points of this fracture, which requires that the number of grid points between two adjacent fractures be at least 4 for second-order extrapolation. That explains why in the region of fractures the number of points per dominant wavelength is relatively large, e.g., no less than 40 in our numerical tests.

#### 4 INTERNAL PROPERTIES OF FAULT ZONES

Fault-zone reflected and transmitted waves can be influenced by the internal structures as well as by the fault-zone geometry. For a fault zone consisting of a system of fractures (cracks) or a complex shear zone, important parameters include fracture strength and fracture spacing.

In the following discussion, these parameters are listed in order of decreasing importance to reflected waves. For example, we discuss the fracture stiffness first since its magnitude varies substantially with different rock samples and it largely governs the magnitude of the waves reflected from fractures.

Here we discuss fault zones consisting of fractures. For discussions on fault zones characterized as low-velocity zones, refer to Igel et al. (1997).

##### 4.1 Fracture stiffness

The fracture strength, or the magnitude of fracture stiffness, can vary over many orders of magnitudes, strongly influencing the magnitude of the reflected waves. Laboratory experiments suggest a range of fracture stiffness from  $10^7$  to  $10^{13}$  Pa/m (Myer, 1998; Schoenberg, 1998; Pyrak-Nolte and Morris, 2000).

Consider an SH-wave in a constant background. According to expression (5), as  $\mathcal{K}_y \rightarrow 0$ , a fracture degenerates to a free surface and the reflection coefficient for displacement approaches unity. As  $\mathcal{K}_y \rightarrow \infty$ , a fracture becomes a welded interface, and the reflection coefficient for displacement approaches 0, as shown in Figure 7. Note that reflection and transmission coefficients shown

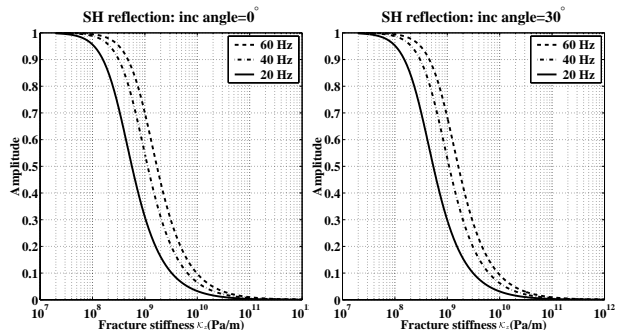


**Figure 7.** Reflection amplitude versus fracture strength for SH reflected waves. Left: normal incidence; right: incidence angle= $30^\circ$ . The medium parameters are constant SH-wave velocity  $\beta=1732$  m/s and constant density  $\rho=1500$  kg/m<sup>3</sup>.

in Figures 7~10 are for the particle displacement (or velocity), not for the potential of the waves.

Now consider P- and SV-waves in constant background. Here we change the normal component of the fracture stiffness  $\mathcal{K}_z$  from  $10^7$  to  $10^{12}$  Pa/m and set the shear component as  $\mathcal{K}_x = \mathcal{K}_z/2$ . When both  $\mathcal{K}_x$  and  $\mathcal{K}_z$  decrease to a small value, e.g.,  $10^7$  Pa/m, the fracture degenerates to a free surface. The reflection coefficient for a P-wave approaches unity for normal incidence. However, for oblique angles, it approaches a value less than 1 because of energy conversion between P- and SV-waves, as shown in Figure 8. For a reflected SV-wave, the reflection coefficient vanishes for normal incidence no matter how large the fracture stiffness, but for oblique angles, it increases because of the energy conversion, as shown in Figure 9.

When both  $\mathcal{K}_x$  and  $\mathcal{K}_z$  increase to a large value, e.g.,  $10^{12}$  Pa/m, the fracture behaves as a welded interface and the reflection coefficients for both P and SV reflections vanish.

For  $\mathcal{K}_x = 0$ , the fracture becomes a hydraulic fracture, which cannot carry any shear stress. Consider the SS transmission coefficients. As shown in Figure 10, for a dry fracture ( $\mathcal{K}_x \neq 0$ ), the SS-transmission coefficients vanish as both  $\mathcal{K}_x$  and  $\mathcal{K}_z$  decrease to a small value, e.g.,  $10^7$  Pa/m and approach unity as both  $\mathcal{K}_x$  and  $\mathcal{K}_z$  increase to a large value, e.g.,  $10^{12}$  Pa/m. For a hydraulic fracture ( $\mathcal{K}_x = 0$ ), however, the SS-transmission coefficients vanish for normal incidence no matter how large the normal component of the fracture stiffness  $\mathcal{K}_z$ , and vary in a small range (e.g.,  $0 \sim 0.2$ ) for oblique angles, which is indicated as shear-wave shadowing (Groenenboom and Fokkema, 1998; Wills et al., 1992).

##### 4.2 Fracture spacing

Fracture spacing has a significant influence on the reflected waves. Here we consider a stack of fractures. All fractures are identical and evenly spaced with the frac-

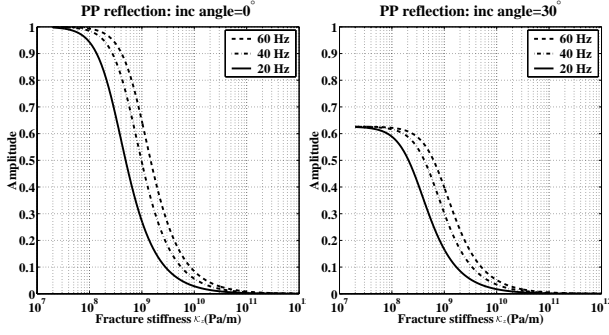


**Figure 8.** Reflection amplitude versus fracture strength for PP reflected waves. Left: normal incidence; right: incidence angle=30°. The medium parameters are constant background velocity, P-wave velocity  $\alpha=3000$  m/s, SV-wave velocity  $\beta=1732$  m/s, constant density  $\rho=1500$  kg/m<sup>3</sup>, and  $\mathcal{K}_x = \mathcal{K}_z/2$ .

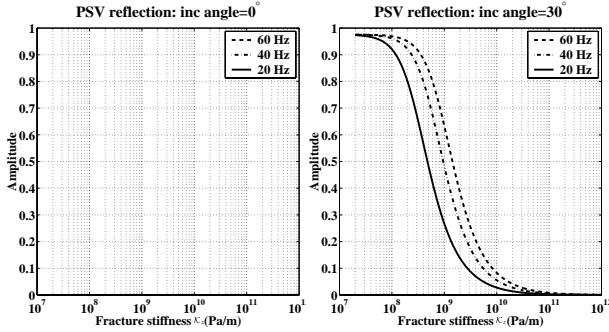


**Figure 9.** Reflection amplitude versus fracture strength for P-SV reflected waves. Left: normal incidence; right: incidence angle=30°. The medium parameters are the same as in Figure 8.

ture spacing much smaller than the dominant seismic wavelength.

To analyze the influence of fracture spacing on reflected waves, we fix the fault-zone width while changing the number of fractures in the zone. Figure 11 shows the configuration of fracture spacing. Waves propagate downward to the fault zone, which consists of horizontal fractures in a constant background medium. As fracture spacing decreases, the number of fractures increases; hence the reflection amplitude increases, as shown in Figure 12.

Figure 13 shows the reflected waveforms for various fracture spacings based on reflection coefficients given by the analytic formulas (B15) in Appendix B. In this analysis, the fault zone width is set as 1 m and the fracture stiffness  $\mathcal{K}_y = 2.096 \times 10^9$  Pa/m. As the fracture spacing decreases from 1 m to 2 cm, more fractures are included in the fault zone, reducing the effective strength of the fault zone and increasing the reflection coefficient. Note that the reflection coefficients also depend on the fault-zone width.

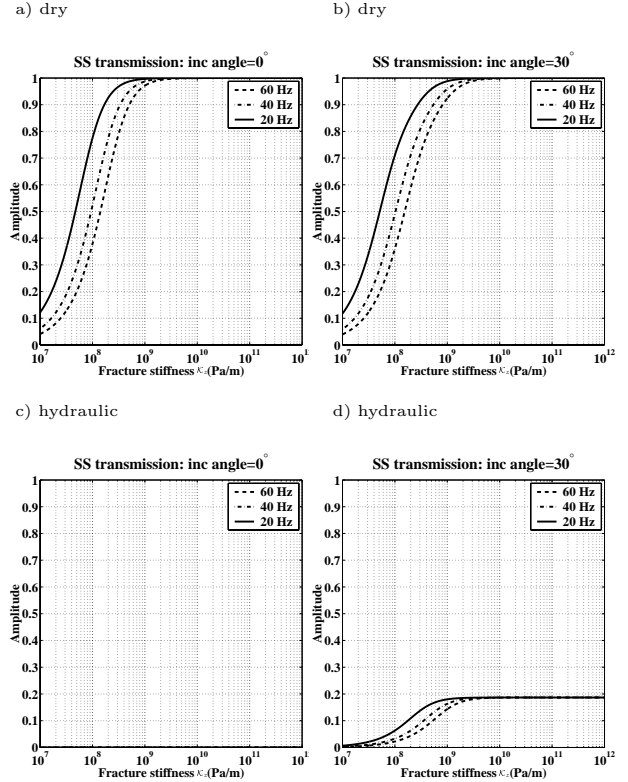


**Figure 10.** Transmission amplitude versus fracture strength for SS transmitted waves: a) dry fracture, incidence angle=0°, b) dry fracture, incidence angle=30°, c) hydraulic fracture, incidence angle=0°, d) hydraulic fracture, incidence angle=30°. For the dry fracture, the medium parameters are the same as in Figure 8; for the hydraulic fracture, the shear component of the fracture stiffness is set at 0.

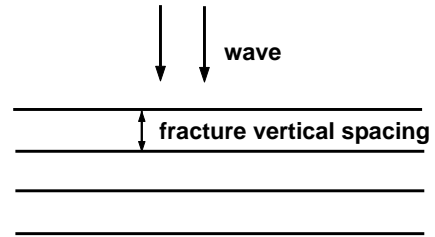


**Figure 11.** Configuration of fracture spacing. All the fractures are identical, horizontal, and densely but evenly distributed. Waves propagate downward to the horizontal fault zone. The medium parameters are constant SH-wave velocity  $\beta=1732$  m/s, constant density  $\rho_1 = \rho_2=1500$  kg/m<sup>3</sup>, and fracture stiffness  $\mathcal{K}_y = 2.096 \times 10^9$  Pa/m. The fault zone width is set as 6 m, and the dominant wavelength of the source is set at 40 Hz.

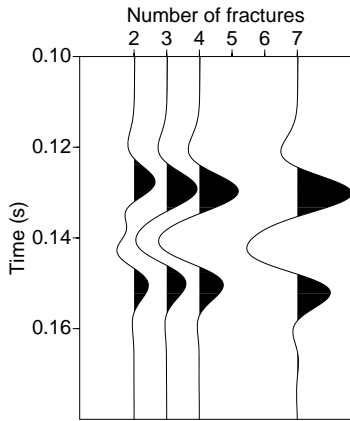


**Figure 12.** Dependence of the waveform and amplitude of SH-waves reflected at normal incidence on fracture spacing. Each trace represents the response from a fault zone with different vertical fracture density.

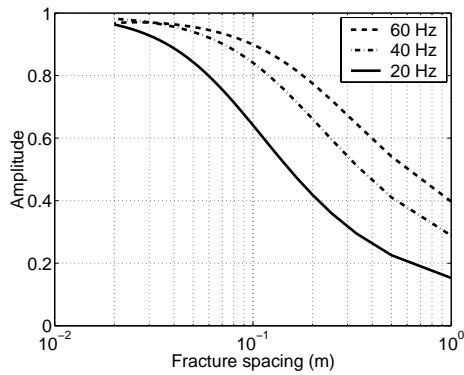


**Figure 13.** SH reflection coefficients at normal incidence for different fracture spacing, based on the analytic solution (B15). Velocity, density, and fracture stiffness are the same as in Figure 11. The fault-zone width is set as 1 m.

### 4.3 Crack distribution pattern

Compared to other properties, the lateral crack distribution pattern has less influence on the reflected waves. Consider a system of parallel cracks with the different distribution patterns shown in Figure 14. All the cracks are identical for all distribution patterns. The horizontal spacing between cracks is set as four times the crack length. In pattern 1, all layers of cracks are identical. In pattern 2, the cracks in each layer shift by one half of the horizontal spacing relative to the layer above. In pattern 3, the cracks in each layer shift by a distance of one crack length relative to the layer above.

Figure 15 shows how the reflected waveform changes with different pattern. The data are noise free. The difference among maximum amplitudes corresponding to different patterns is only 20% in this numerical

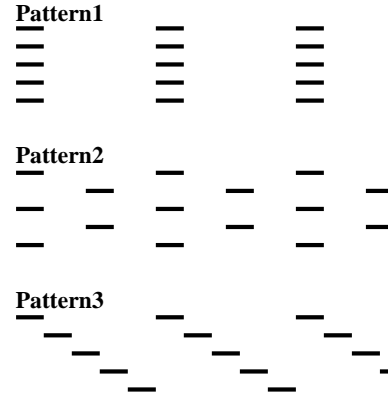


**Figure 14.** Different distribution patterns of cracks. The horizontal spacing between cracks is set as four times the crack length. Cracks are closely distributed.

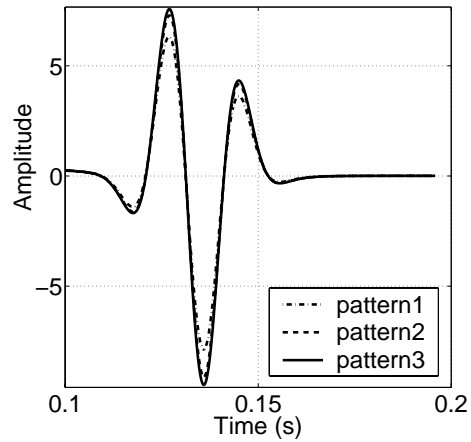


**Figure 15.** Influence of crack distribution pattern on SH reflected waveform (particle velocity  $v_y$ ).

test; in practice, such a small amplitude variation will often be obscured by noise.

### 4.4 Random variation

The least important properties for waves reflected from fault zones is the small-scale random variation in density and velocity, or in fracture stiffness. Figure 16 shows SH reflected waveforms for different internal structures of a fault zone. In plots a) and b), waveforms are compared for a constant low-velocity layer and a low-velocity layer with 25% of Gaussian distribution added to the constant background velocity in the layer. No significant change is observed for the two zones.

Similar results hold for the fault zone consisting of cracks, as shown in plots c) and d). Only a negligible change on the wavefield is detected. The waveshape of the reflection keeps almost unaltered. The results suggest that small-scale structure (compared to the dominant wavelength) in the complex shear zone can be



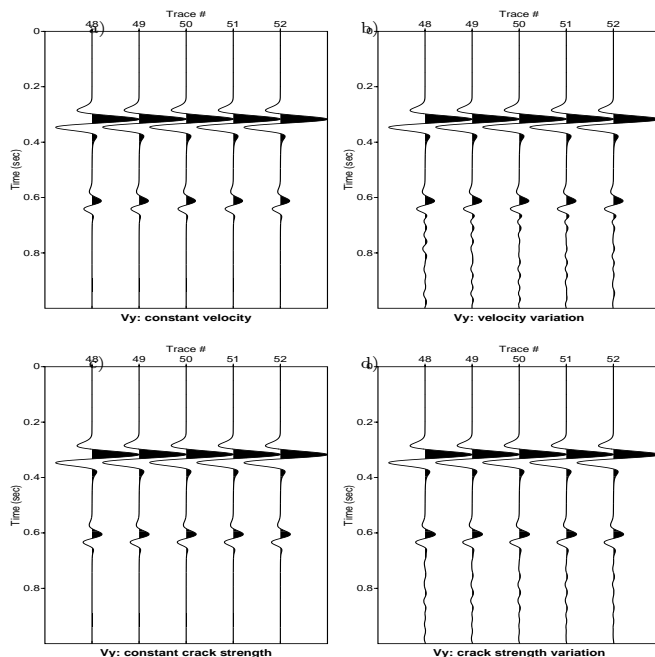


**Figure 16.** SH reflected waveforms (particle velocity  $V_y$ ) for different internal structure of a fault zone: a) constant low-velocity layer, b) low-velocity layer with 25% of Gaussian distribution added to the constant background velocity in the layer, c) layer filled with cracks with constant fracture stiffness, d) layer filled with cracks with 25% of Gaussian distribution added to the fracture stiffness.

largely smoothed out and modeled with equivalent media in the observed range of wavelengths.

## 5 DISCUSSION AND CONCLUSIONS

Reflected and transmitted waves provide a potential tool for diagnosing fault zones when trapped waves cannot be measured. Studies based on fault-zone trapped waves, carried out for large-scale tectonic fault zones, give estimates of the shear velocities in fault zones (Li et al., 1994). In the interpretation of fault zones close to a reservoir, fracture strength and density, among other factors, hold the key for the ability of a fault zone to excite reflected and transmitted waves.

A fault zone, whether characterized as a low-velocity layer or comprised of fractures, can excite significant reflected and transmitted waves. Apart from changing the amplitudes of reflected and transmitted waves, fault zones characterized as either a low-velocity zone or fracture (crack) systems modify the phase of the waveform and make the seismic response frequency-dependent.

Using the staggered-grid finite-difference, we developed an extrapolation scheme for simulating wave prop-

agation influenced by fractures described as linear slip boundaries. In the update of the stresses at each time step in the region of fractures, particle velocities are extrapolated from neighboring points to the point where stresses need to be evaluated and the difference between the extrapolated particle velocities across the fracture is calculated to get the time derivative of the stress. To make the extrapolation stable, relationship between the stress and particle velocity are taken as constraints on the extrapolation. Two  $9 \times 9$  linear systems are designed for evaluating the particle velocities and stresses at the fracture interface, one for  $v_x$  and  $\tau_{xz}$  and another for  $v_z$  and  $\tau_{zz}$ . Wherever the fracture stiffnesses and the background medium parameters stay the same along the fractures, only two  $9 \times 9$  linear systems are required; otherwise different  $9 \times 9$  linear systems need to be solved for each grid point on the fracture where either the fracture stiffness or the background medium parameter changes. Since all the linear systems are time-invariant and need to be solved only once, extra computation cost for simulating the fractures are negligible. Numerical examples support the validity of this approach. A standard staggered-grid scheme is applied to regions where there is no fracture.

We discussed relative importance of internal properties of fault zones on reflected waves. Fracture stiffness and fracture spacing change significantly the magnitude of the waves, while crack distribution pattern and small-scale random variation on velocity or fracture stiffness have little influence on the wavefields; hence, fault zones can be modeled with equivalent media in a typical range of seismic wavelengths. Another important factor, crack orientation, is not covered in this paper.

## 6 ACKNOWLEDGMENTS

The authors would like to thank Mike Batzle, Robert Kranz, Matt Haney, and Reynaldo Cardona for valuable discussion on fractures in rocks, and Junping Wang for discussion on numerical issues.

## 7 REFERENCES

- Aki, K., and Richards, P. G., 1980, Quantitative seismology: theory and methods: University Science Books, California.
- Chaisri, S., and Krebs, E. S., 2000, Exact and approximate formulas for P-SV reflection and transmission coefficients for a nonwelded contact interface: *J. Geophys. Res.*, **105**, 28045–28054.
- Coates, R. T., and Schoenberg, M., 1995, Finite-difference modeling of faults and fractures: *Geophysics*, **60**, 1514–1526.
- Fan, J., Gu, B., Nihei, K. T., Cook, N. G. W., and

Myer, L. R., 1996, Experimental and numerical investigation of fracture interface waves: *Rock Mechanics*, Balkema, Rotterdam, 845–851.

Groenenboom, J., and Fokkema J.T., 1998, Monitoring the width of hydraulic fractures with acoustic waves: *Geophysics*, **63**, 139–148.

Igel, H., Ben-Zion, Y., and Leary, P. C., 1997, Simulation of SH- and P-SV- wave propagation in fault zones: *Geophys. J. Int.*, **128**, 533–546.

Igel, H., Jahnke, G., and Ben-Zion, Y., 2001, Numerical simulation of fault zone guided waves: accuracy and 3-D effects: *PAGEOPH*, in press.

Li, Y. G., Leary, P., Aki, K., and Malin, P., 1990, Seismic trapped modes in the Oroville and San Andreas fault zones: *Science*, **249**, 763–765.

Li, Y. G., Aki, K., Adams, D., and Hasemi, A., 1994, Seismic guided waves trapped in the fault zone of the Landers, California, earthquake of 1992: *J. Geophys. Res.*, **99**, 11705–11722.

Li, Y. G., Vidale, J. E., Aki, K., Marone, C. J., and Lee, W. H., 1994, Fine structure of the Landers fault zone: segmentation and the rupture process: *Science*, **265**, 367–370.

Li, Y. G., Vidale, J. E., 1996, Low-velocity fault-zone guided waves: Numerical investigations of trapping efficiency: *Bulletin of the Seismological Society of America*, **86**, 371–378.

Myer, L., 1998, Seismic wave propagation in fractured rock, *in* Rossmannith, Ed., *Mechanics of jointed and faulted rock*, Balkema, Rotterdam, 29–38.

Pyrak-Nolte, L. J., Myer, L.R., and Cook, N.G.W., 1990a, Anisotropy in seismic velocities and amplitudes from multiple parallel fractures: *J. Geophys. Res.*, **95**, 11345–11358.

Pyrak-Nolte, L. J., Myer, L.R., and Cook, N.G.W., 1990b, Transmission of seismic waves across single natural fractures: *J. Geophys. Res.*, **95**, 8617–8638.

Pyrak-Nolte, L. J., Xu, J., and Haley, G. M., 1992, Elastic interface waves along a fracture: Theory and experiment, *in* Tillerson and Wawersik, Eds., *Rock Mechanics*, Balkema, Rotterdam, 999–1007.

Pyrak-Nolte, L. J., 1996, The seismic response of fractures and the interrelations among fracture properties: *Int. J. Rock Mech. Min. Sci. and Geomech. Abstr.*, **33**, 787–802.

Pyrak-Nolte, L. J., and Morris, J. P., 2000, Single fractures under normal stress: The relation between fracture specific stiffness and fluid flow: *Int. J. Rock Mech. Min. Sci. and Mining Sciences*, **37**, 245–262.

Reid, W. F., Cosentino, R.D., Harris, T. B., and Baldwin, J. N., 2002, Shallow seismic reflection imaging of the Idalia Hill fault zone, southeastern Missouri: North-Central Section (36th) and Southeastern Section (51st), *GSA Joint Annual Meeting* (April 3-5, 2002).

Schoenberg, M., 1980, Elastic wave behavior across linear slip interfaces: *J. Acoust. Soc. Am.*, **68**, 1516–1521.

Schoenberg, M., 1998, Acoustic characterization of underground fractures: *Ann. Internat. Mtg., Soc. Expl. Geophys.*, Expanded Abstracts.

Snieder, R., 2001, A guided tour of mathematical methods for the physical sciences: Cambridge University Press.

Sánchez-Sesma, F. J., and Iturrarán-Viveros, U., 2001, Scattering and diffraction of SH waves by a finite crack: an analytical solution: *Geophysical Journal International*, **145**, 749–758.

Terzaghi, K., 1936, The shearing resistance of saturated soils: *Proc. of the First International Conference on Soil Mechanics and Foundation Engineering*, **1**, 54–56.

Virieux, J., 1984, SH-wave propagation in heterogeneous media: Velocity-stress finite-difference method: *Geophysics*, **49**, 1933–1957.

Virieux, J., 1986, P-SV wave propagation in heterogeneous media: Velocity-stress finite-difference method: *Geophysics*, **51**, 889–901.

Wills, P. B., DeMartini D. C., Vinegar H. J., Shlyapobersky, J., Deeg, W. F., Woerpel, J. C., Fix, J. E., Sorrells, G. G., and Adair, R. G., 1992, Active and passive imaging of hydraulic fractures: *The Leading Edge*, **11**, 15–22.

Yi, W., Nakagawa, S., Nihei, K.T., 1998, Numerical investigation of fracture channel waves: *Ann. Internat. Mtg., Soc. Expl. Geophys.*, Expanded Abstracts.

## APPENDIX A: EXTRAPOLATION SCHEME FOR THE FINITE DIFFERENCE SIMULATION OF FRACTURES ON A STAGGERED-GRID

Consider the velocity-stress representation of a 2-D wave equation. In the presence of a horizontal fracture (in  $x$ -direction), we have

$$\begin{aligned} \frac{\partial v_x}{\partial t} &= \frac{1}{\rho} \left( \frac{\partial \tau_{xx}}{\partial x} + \frac{\partial \tau_{xz}}{\partial z} \right), \\ \frac{\partial v_z}{\partial t} &= \frac{1}{\rho} \left( \frac{\partial \tau_{xz}}{\partial x} + \frac{\partial \tau_{zz}}{\partial z} \right), \\ \frac{\partial \tau_{xx}}{\partial t} &= (\lambda + 2\mu) \frac{\partial v_x}{\partial x} + \lambda \frac{\partial v_z}{\partial z}, \\ \frac{\partial \tau_{zz}}{\partial t} &= \mathcal{K}_z[v_z], \\ \frac{\partial \tau_{xz}}{\partial t} &= \mathcal{K}_x[v_x], \end{aligned} \tag{A1}$$

where  $v$  denotes the particle velocity,  $\tau$  denotes the stress, and  $\lambda$  and  $\mu$  are the Lamé parameters. The square brackets here denote the difference between the particle velocities across the fracture interface.

In the calculation of the stresses given by expression (A1), we extrapolate the particle velocity from neighboring points to the point where the stress needs to be evaluated as illustrated in Figure A1, to calculate

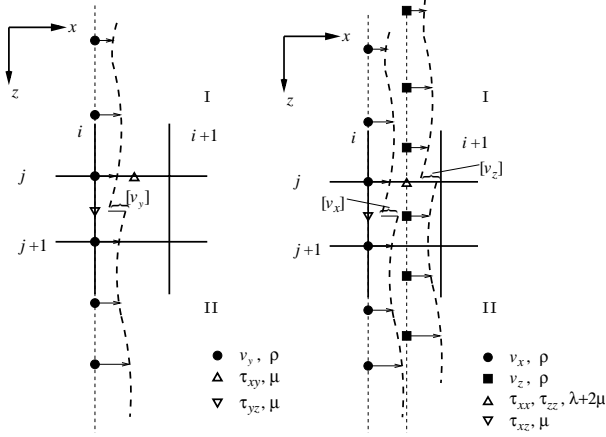


**Figure A1.** Staggered grid used in handling the elastic boundary condition, shown in expression (1), in the elastic finite-difference calculations.  $i$  and  $i + 1$  denote the index of the nodes on the grid in the  $x$  direction;  $j$  and  $j + 1$  denote the index of the nodes on the grid in the  $z$  direction. Thick dashed curves denote the magnitude of the particle velocities, and the square brackets denote the difference between the displacements above and below the fracture. The particle velocities at neighboring points are extrapolated to the point where the stress component needs to be evaluated. Left: modeling the SH-wave where the stress component  $\tau_{yz}$  is calculated based on the difference between the particle displacements, which are the time integral of the difference between the particle velocities,  $[v_y]$ . Right: modeling the P-SV waves where the stress components  $\tau_{xz}$  and  $\tau_{zz}$  are calculated based on the difference between the particle displacements which are the time integrals of the difference between the particle velocities,  $[v_x]$  and  $[v_z]$ , respectively. A polynomial extrapolation technique is used.

the difference between the extrapolated particle velocities across the fracture, which accounts for the time derivative of the stress, and finally to get the updated stress at that point.

A direct extrapolation would be a natural way to evaluate the stresses at the fracture interface, but it is not constrained since different extrapolation schemes lead to different value of the particle velocities, which greatly change the value of stresses. Hence further constraints need to be considered. Our approach is to extrapolate the particle velocity to the fracture interface while taking the relationship between the stress and particle velocity as a constraint on the extrapolation.

For medium I, two second-order polynomials are used to approximate the particle velocities near the fracture. Hence we have

$$\begin{aligned} az_{j-1}^2 + bz_{j-1} + c &= v_{xj-1}, \\ az_j^2 + bz_j + c &= v_{xj}, \\ az_{j+\frac{1}{2}}^2 + bz_{j+\frac{1}{2}} + c &= v_{xj+\frac{1}{2}}^I, \end{aligned} \quad (\text{A2})$$

for the particle velocity  $v_x$  and

$$\begin{aligned} a'z_{j-\frac{3}{2}}^2 + b'z_{j-\frac{3}{2}} + c' &= v_{zj-\frac{3}{2}}, \\ a'z_{j-\frac{1}{2}}^2 + b'z_{j-\frac{1}{2}} + c' &= v_{zj-\frac{1}{2}}, \\ a'z_j^2 + b'z_j + c' &= v_{zj}^I, \end{aligned} \quad (\text{A3})$$

for the particle velocity  $v_z$ . The stress components  $\tau_{xz}$  and  $\tau_{zz}$  are governed by the following constituent relationship

$$\begin{aligned} \left(\frac{\partial \tau_{xz}}{\partial t}\right)_{j+\frac{1}{2}} &= \mu_{j+\frac{1}{2}}(2az_{j+\frac{1}{2}} + b) + \mu_{j+\frac{1}{2}}\left(\frac{\partial v_z}{\partial x}\right)_{j+\frac{1}{2}}, \\ \left(\frac{\partial \tau_{zz}}{\partial t}\right)_j &= (\lambda_j + 2\mu_j)(2a'z_j + b') + \lambda_j\left(\frac{\partial v_x}{\partial x}\right)_j. \end{aligned} \quad (\text{A4})$$

where  $a$  through  $c$  and  $a'$  through  $c'$  are coefficients of the second-order polynomials.

Similarly, for medium II we have

$$\begin{aligned} dz_{j+1}^2 + ez_{j+1} + f &= v_{xj+1}, \\ dz_{j+2}^2 + ez_{j+2} + f &= v_{xj+2}, \\ dz_{j+\frac{1}{2}}^2 + ez_{j+\frac{1}{2}} + f &= v_{xj+\frac{1}{2}}^{II}, \end{aligned} \quad (\text{A5})$$

for the particle velocity  $v_x$ ,

$$\begin{aligned} d'z_{j+\frac{1}{2}}^2 + e'z_{j+\frac{1}{2}} + f' &= v_{zj+\frac{1}{2}}, \\ d'z_{j+\frac{3}{2}}^2 + e'z_{j+\frac{3}{2}} + f' &= v_{zj+\frac{3}{2}}, \\ d'z_j^2 + e'z_j + f' &= v_{zj}^{II}, \end{aligned} \quad (\text{A6})$$

for the particle velocity  $v_z$ , and

$$\begin{aligned} \left(\frac{\partial \tau_{xz}}{\partial t}\right)_{j+\frac{1}{2}} &= \mu_{j+\frac{1}{2}}(2dz_{j+\frac{1}{2}} + e) + \mu_{j+\frac{1}{2}}\left(\frac{\partial v_z}{\partial x}\right)_{j+\frac{1}{2}}, \\ \left(\frac{\partial \tau_{zz}}{\partial t}\right)_j &= (\lambda_j + 2\mu_j)(2d'z_j + e') + \lambda_j\left(\frac{\partial v_x}{\partial x}\right)_j. \end{aligned} \quad (\text{A7})$$

where  $d$  through  $f$  and  $d'$  through  $f'$  are coefficients of the second-order polynomials.

Furthermore, the stress components  $\tau_{xz}$  and  $\tau_{zz}$  are governed by the difference between particle displacements (and hence particle velocities) across the fracture interface

$$\begin{aligned} \left(\frac{\partial \tau_{xz}}{\partial t}\right)_{j+\frac{1}{2}} &= \mathcal{K}_{xj+\frac{1}{2}}[v_x]_{j+\frac{1}{2}} = \mathcal{K}_{xj+\frac{1}{2}}(v_{xj+\frac{1}{2}}^{II} - v_{xj+\frac{1}{2}}^I), \\ \left(\frac{\partial \tau_{zz}}{\partial t}\right)_j &= \mathcal{K}_{zj}[v_z]_j = \mathcal{K}_{zj}(v_{zj}^{II} - v_{zj}^I). \end{aligned} \quad (\text{A8})$$

Re-organizing the above expressions (A2~A8) leads to two  $9 \times 9$  linear systems:

$$\begin{aligned} az_{j-1}^2 + bz_{j-1} + c &= v_{xj-1}, \\ az_j^2 + bz_j + c &= v_{xj}, \\ az_{j+\frac{1}{2}}^2 + bz_{j+\frac{1}{2}} + c &= v_{xj+\frac{1}{2}}^I, \\ dz_{j+1}^2 + ez_{j+1} + f &= v_{xj+1}, \\ dz_{j+2}^2 + ez_{j+2} + f &= v_{xj+2}, \\ dz_{j+\frac{1}{2}}^2 + ez_{j+\frac{1}{2}} + f &= v_{xj+\frac{1}{2}}^{II}, \end{aligned} \quad (\text{A9})$$

$$\left(\frac{\partial \hat{\tau}_{xz}}{\partial t}\right)_{j+\frac{1}{2}} = (2az_{j+\frac{1}{2}} + b) + \left(\frac{\partial v_z}{\partial x}\right)_{j+\frac{1}{2}},$$

$$\begin{aligned} \left(\frac{\partial \hat{\tau}_{xz}}{\partial t}\right)_{j+\frac{1}{2}} &= (2dz_{j+\frac{1}{2}} + e) + \left(\frac{\partial v_z}{\partial x}\right)_{j+\frac{1}{2}}, \\ \left(\frac{\partial \hat{\tau}_{xz}}{\partial t}\right)_{j+\frac{1}{2}} &= \frac{\mathcal{K}_{xj+\frac{1}{2}}}{\mu_{j+\frac{1}{2}}}(v_{xj+\frac{1}{2}}^{II} - v_{xj+\frac{1}{2}}^I), \end{aligned}$$

where the nine unknowns are  $a$  through  $f$ ,  $v_{xj+\frac{1}{2}}^I$ ,  $v_{xj+\frac{1}{2}}^{II}$ , and  $\left(\frac{\partial \tau_{xz}}{\partial t}\right)_{j+\frac{1}{2}}$ , and

$$\begin{aligned} a'z_{j-\frac{3}{2}}^2 + b'z_{j-\frac{3}{2}} + c' &= v_{zj-\frac{3}{2}}, \\ a'z_{j-\frac{1}{2}}^2 + b'z_{j-\frac{1}{2}} + c' &= v_{zj-\frac{1}{2}}, \\ a'z_j^2 + b'z_j + c' &= v_{zj}^I, \\ d'z_{j+\frac{1}{2}}^2 + e'z_{j+\frac{1}{2}} + f' &= v_{zj+\frac{1}{2}}, \\ d'z_{j+\frac{3}{2}}^2 + e'z_{j+\frac{3}{2}} + f' &= v_{zj+\frac{3}{2}}, \\ d'z_j^2 + e'z_j + f' &= v_{zj}^{II}, \end{aligned} \quad (\text{A10})$$

$$\begin{aligned} \left(\frac{\partial \hat{\tau}_{zz}}{\partial t}\right)_j &= (2a'z_j + b') + \frac{\lambda_j}{(\lambda_j + 2\mu_j)}\left(\frac{\partial v_x}{\partial x}\right)_j, \\ \left(\frac{\partial \hat{\tau}_{zz}}{\partial t}\right)_j &= (2d'z_j + e') + \frac{\lambda_j}{(\lambda_j + 2\mu_j)}\left(\frac{\partial v_x}{\partial x}\right)_j, \\ \left(\frac{\partial \hat{\tau}_{zz}}{\partial t}\right)_j &= \frac{\mathcal{K}_{zj}}{(\lambda_j + 2\mu_j)}(v_{zj}^{II} - v_{zj}^I), \end{aligned}$$

where the nine unknowns are  $a'$  through  $f'$ ,  $v_{zj}^I$ ,  $v_{zj}^{II}$ , and  $\left(\frac{\partial \tau_{zz}}{\partial t}\right)_j$ . The stress components are normalized by the Lamé parameters:  $\hat{\tau}_{xz} = \frac{\tau_{xz}}{\mu_j}$  and  $\hat{\tau}_{zz} = \frac{\tau_{zz}}{(\lambda + 2\mu)}$ .

## APPENDIX B: SH REFLECTION AND TRANSMISSION COEFFICIENTS FOR A STACK OF FRACTURES

### B1 SH reflection and transmission coefficients for two parallel fractures

Here we consider two identical, parallel fractures with infinite length. The spacing between these two fractures is denoted as  $d$ . The fracture stiffness is denoted as  $\mathcal{K}_y$ . The parameters of the media above and below the layer are denoted by index 1 and 2, respectively, while parameters of the layer bounded by the two fractures are denoted by index 3.

Summing over all possible intra-bed multiples in the layer yields

$$\begin{aligned} R &= R_{13} + T_{13}D^2R_{32}T_{31} + T_{13}D^4R_{32}^2R_{31}T_{31} + \\ &\quad T_{13}D^6R_{32}^3R_{31}^2T_{31} + \dots \\ &= R_{13} + \frac{T_{13}D^2R_{32}T_{31}}{1 - D^2R_{32}R_{31}}, \end{aligned} \quad (\text{B1})$$

$$\begin{aligned} T &= T_{13}DT_{32} + T_{13}D^3R_{32}R_{31}T_{32} + \\ &\quad T_{13}D^5R_{32}^2R_{31}^2T_{32} + \dots \\ &= \frac{T_{13}DT_{32}}{1 - D^2R_{32}R_{31}}, \end{aligned} \quad (\text{B2})$$

where  $D = e^{i\omega \cos j_3 d / \beta_3}$  denotes the phase shift of waves

propagating in the bounded layer. Reflection and transmission coefficients from different boundaries are given by

$$R_{13} = \frac{(Z_1 - Z_3) - iZ_1Z_3\frac{\omega}{\mathcal{K}_y}}{(Z_1 + Z_3) - iZ_1Z_3\frac{\omega}{\mathcal{K}_y}}, \quad (\text{B3})$$

$$R_{31} = \frac{(Z_3 - Z_1) - iZ_3Z_1\frac{\omega}{\mathcal{K}_y}}{(Z_3 + Z_1) - iZ_3Z_1\frac{\omega}{\mathcal{K}_y}}, \quad (\text{B4})$$

$$T_{13} = \frac{2Z_1}{(Z_1 + Z_3) - iZ_1Z_3\frac{\omega}{\mathcal{K}_y}}, \quad (\text{B5})$$

$$T_{31} = \frac{2Z_3}{(Z_3 + Z_1) - iZ_3Z_1\frac{\omega}{\mathcal{K}_y}}, \quad (\text{B6})$$

$$R_{32} = \frac{(Z_3 - Z_2) - iZ_3Z_2\frac{\omega}{\mathcal{K}_y}}{(Z_3 + Z_2) - iZ_3Z_2\frac{\omega}{\mathcal{K}_y}}, \quad (\text{B7})$$

$$T_{32} = \frac{2Z_3}{(Z_3 + Z_2) - iZ_3Z_2\frac{\omega}{\mathcal{K}_y}}, \quad (\text{B8})$$

where  $\omega$  denotes the angular frequency,  $Z_m = \rho_m \beta_m \cos j_m$  denotes the impedance in medium  $m$ , and  $j$  denotes the angle that SH waves make with the normal to the fracture interface. For reflection and transmission coefficients, the first index denotes the incident medium, and the second index denotes the medium where the reflected and transmitted waves propagate.

In the special case of constant background ( $\rho_1 = \rho_2 = \rho_3 = \rho$ ,  $\beta_1 = \beta_2 = \beta_3 = \beta$ , and hence  $j_1 = j_2 = j_3 = j$ ), we have

$$R_{13} = R_{31} = R_{32} = \frac{-iZ\frac{\omega}{\mathcal{K}_y}}{2 - iZ\frac{\omega}{\mathcal{K}_y}} = \frac{-iB}{2 - iB}, \quad (\text{B9})$$

$$T_{13} = T_{31} = T_{32} = \frac{2}{2 - iZ\frac{\omega}{\mathcal{K}_y}} = \frac{2}{2 - iB}. \quad (\text{B10})$$

where  $Z = \rho\beta \cos j$  denotes the impedance and  $B = Z\frac{\omega}{\mathcal{K}_y}$ .

Introducing expressions (B9) and (B10) into (B1) and (B2) yields

$$R = \frac{-iB}{2 - iB} \frac{(2 - iB)^2 + B^2D^2 + 4D^2}{(2 - iB)^2 + B^2D^2}, \quad (\text{B11})$$

$$T = \frac{4D}{(2 - iB)^2 + B^2D^2}. \quad (\text{B12})$$

When the fracture spacing  $d$  is much smaller than the wavelength, the phase shift term  $D \approx 1 + i\frac{\omega \cos jd}{\beta}$ .

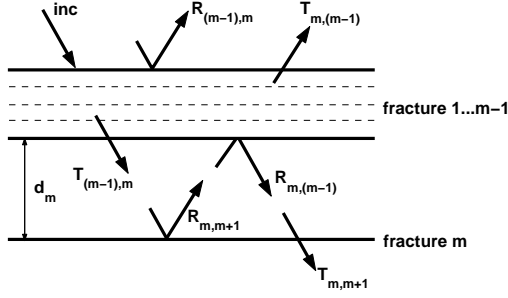


**Figure A2.** Configuration of a stack of fractures. All fractures are identical, parallel and evenly spaced. Parameters of the medium between fracture  $m - 1$  and  $m$  are fracture spacing  $d_m$ , SH-wave velocity  $\beta_m$ , and density  $\rho_m$ . Brackets denote fractures 1 through  $m - 1$ .

Hence we have

$$R = \frac{-iB}{2 - iB} \frac{2 - 2iB + B^2 \frac{\omega \cos jd}{\beta} + 4 \frac{\omega \cos jd}{\beta}}{2 - 2iB + B^2 \frac{\omega \cos jd}{\beta}}, \quad (\text{B13})$$

$$T = \frac{2 \frac{\omega \cos jd}{\beta}}{2 - 2iB + B^2 \frac{\omega \cos jd}{\beta}}. \quad (\text{B14})$$

## B2 SH reflection and transmission coefficients for a stack of fractures

For a stack of fractures, the reflection and transmission coefficients can be derived recursively. Suppose the reflection and transmission coefficients for fractures 1 through  $m - 1$  are  $R_{(m-1),m}$ ,  $R_{m,(m-1)}$ ,  $T_{(m-1),m}$ , and  $T_{m,(m-1)}$ , respectively, where the first index denotes the incident medium and the second index denotes the reflecting or transmitting medium, and brackets denote fractures 1 through  $m - 1$ , as shown in Figure A2.

Hence the reflection and transmission coefficients for the system consisting of fractures 1 through  $m$  are (Snieder, 2001)

$$R_{(m),m+1} = R_{(m-1),m} + \frac{T_{(m-1),m} D^2 R_{m,m+1} T_{m,(m-1)}}{1 - D^2 R_{m,m+1} R_{m,(m-1)}}, \quad (\text{B15})$$

$$T_{(m),m+1} = \frac{T_{(m-1),m} D T_{m,m+1}}{1 - D^2 R_{m,m+1} R_{m,(m-1)}}, \quad (\text{B16})$$

where  $D = e^{i\omega \cos j_m d / \beta_m}$  denotes the phase shift of waves propagating in the medium between fracture  $m - 1$  and  $m$ .

